Separation mechanism and influential factor study on vane-type-associated petroleum gas separator

Shuo Liu[a], Jian Zhang[a], Li-Song Wang[a,b], Jing-Yu Xu[a,b,*]

[a] *Institute of Mechanics, Chinese Academy of Sciences, Beijing 100190, China*
[b] *School of Engineering Sciences, University of Chinese Academy of Sciences, Beijing 100049, China*

ABSTRACT

To investigate the separation mechanism of a vane-type separator, a flow experiment and a numerical simulation were conducted. Electrical resistance tomography and Coriolis mass flow meters were used during the flow experiment. An Eulerian multiphase model coupled with the Reynolds stress turbulent model was applied to conduct a corresponding numerical simulation. Based on the phase, the velocity, and the swirling intensity distribution, the separation performance of the separator was discussed in terms of the separation efficiency, the entrainment ratio, and the critical split ratio. Results showed that the swirling intensity was sensitive to the separator geometry and operating parameters. The separation efficiency increased with the split ratio under fixed entrance conditions. Once the split ratio was larger than the critical split ratio, the gas phase collected becomes maximal with a larger liquid phase collected in the branch exit if the split ratio increased continuously. Subsequently, based on the definition of split flow face, the gas–liquid separation mechanism was revealed by discussing the relative location of the gas–liquid interface and the split flow face. Finally, the relationships among the operating parameters including the exit pressure difference, the split ratio, and the liquid phase flow rate were analyzed based on the proposed separation mechanism model. This study provides a better understanding of the vane-type gas–liquid separation procedure and optimization.

1. Introduction

In petroleum extraction, associated petroleum gas (APG) is a side-product of oil extraction and comprises primarily of methane and heavier hydrocarbons [12]. APG is traditionally burned in flares as waste. However, the emission of unburned fuel and the byproducts from combustion (such as CO and NO) cause environmental and health problems, and activities have been implemented to solve them [9]. Despite its burning flare, APG can be collected and applied for energy needs in remote fields and offshore platforms. In recent years, APG application technology has been applied, including the oxycracking of energy fuel for electricity generation [1] and gas-to-liquid conversion to yield synthetic fuel [17]. Hence, for environmental and economic purposes, development of separation mechanism and technology of APG from produced fluids have become more important.

Separating APG from the produced fluids is a gas–liquid separation procedure. Gas–liquid separation technology has been reformed considerably from gravity to centrifugal separation. Researchers have extensively investigated passive cyclone separation using various research methods. In terms of theoretical deduction, an initial swirl number

[26,27] has been proposed for the design of vane curves or cyclone structures. Laser Doppler velocimetry has been applied experimentally for cyclone velocity distribution measurement [7], whereas wire mesh sensors [11] and electrical resistance tomography [5] have been applied to measure section phase holdup. Furthermore, the Malvern droplet size analyzer has been applied for droplet size distribution measurement [5]. When conducting gas–liquid two-phase numerical simulations, both Eulerian–Eulerian [6] and Eulerian–Lagrange approaches [5] have been applied.

For tangential-induced cyclones, the gas–liquid cylindrical cyclone (GLCC) separator is a representative apparatus that has garnered considerable attention from both academia and industry [27]. Heriz et al. [7] applied laser Doppler velocimetry to measure the velocity distribution in GLCC separators and elucidate the origin of double-axial flow reversal in swirling flows. Kanshio et al. [11] tested water hold up in various locations of a GLCC separator using a wire mesh sensor to reconstruct the water-phase distribution. Yue et al. [27] conducted a systematic study on the flow type of upper swirling liquid films and gained a comprehensive understanding of their flow regimes, influence factors, and flow mechanisms.

Another type of passive cyclone is the axial-induced cyclone. It exhibits excellent performances in terms of space demand, pressure drop, and structural complexity [3]. Furthermore, it is particularly suitable to satisfy compact space demands, such as offshore platforms. Axial gas–liquid separators can be classified based on the feeding gas volume fraction. Separator designs and separation mechanisms depend on the feeding gas volume fraction conditions. For conditions where the gas phase is the primary phase and the liquid phase exists in the form of droplets, the separation mechanism focuses on the collection of droplets or film, also known as wet–gas separation. Under this condition, Huang et al. [8] proposed a liquid reservoir to collect the minor liquid phase, whereas Wei et al. [23] proposed narrow tangential conduits to collect droplets and films. Additionally, centrifugal device varies from planar vanes [23] to swirling vanes [13]. Researchers have developed a bubble separator to be applied in a thorium molten salt reactor [21] when the gas phase is minor (volume fraction smaller than 4%) and exists in the form of bubbles at the separator entrance. The bubble separator contains a recovery vane and gas is collected through a hole in the recovery vane hub or the entrance vane hole under different modes. The vane-type separation schemes above may not include all gas–liquid ratio conditions. For conditions where the APG volume fraction is larger than the bubble separator while the liquid is still the primary phase (5–30%), the separator should be changed according to the separation mechanism. However, although records pertaining to the effect of gas core on liquid–solid separation [20] exist, the detailed mechanism of vane-type gas–liquid separation still requires further investigation.

Hence, based on APG separation from produced fluids, a study pertaining to the separation mechanism and influential factor will be conducted based on our previous study [15,19]. Experimental research and CFD (Computational Fluid Dynamics) investigations were conducted in this study, and a separation mechanism model was proposed to detect gas–liquid swirling flow characteristics and swirling intensity variations. In particularly, a flow experiment involving the use of a pressure difference gauge and electrical resistance tomography (ERT) to investigate separation performances and gas phase distributions was conducted. In the numerical simulation conducted, the Reynolds stress model (RSM) coupled with the Eulerian multiphase model were used to reveal gas–liquid flow domain characteristics in the separator. Subsequently, using a separation mechanism model, the relationship between operating parameters was discussed. The methods above contribute significantly to the comprehension and further optimization of vane-type degassing separators applied for APG separation.

2. Experimental description

2.1. Separator configuration

The configuration of the gas–liquid separator is shown in Fig. 1, in which the separator comprised four parts: vane, developing, necking, and separation zones. To avoid discrepancies induced by the geometry scale, such as flow pattern variances, a separator model with scale similar to the equipment used on site was applied in this study. The vane

Table 1
The parameters of separator configuration.

Part	Parameter	Units	Value
Blades and hub	h_1	mm	80
	b	mm	110
	h_2	mm	60
	d_h	mm	50
	φ	°	45°
	γ	°	60°
Separator	H_0	mm	390
	H_1	mm	1000
	H_2	mm	150
	H_3	mm	270
	H_4	mm	240
	H_5	mm	160
	L_1	mm	210
	L_2	mm	400
	D_1	mm	100
	D_2	mm	80
	D_3	mm	65
	d	mm	25

zone was designed to induce a vortex. Its key component included blades and a hub. The blades were mounted centrosymmetrically on the hub. The blade configuration was designed in reference to Cai's [3] optimization work. As shown in Fig. 1 and Table 1, the angle φ which referred to angle between tangential exit and entrance of a blade was 45°, whereas the rotation angle γ was 60°. The thicknesses of the blades were 5 mm each, whereas the diameter of hub was 50 mm.

The developing zone, which contained two pipes, was designed for the gas-phase forming core and stabilization. The longer pipe measured 0.7 m, whereas the shorter measured 0.3 m, which can be replaced by ERT electrodes in the test. The necking zone was designed to accelerate the mixture fluids. The pipe diameter necked downstream from 100 to 80 mm at an axial distance of 150 mm. At 270 mm downstream of the necking zone, a 240-mm-long phase collection pipe along the axial direction was mounted at the center of the pipe. The phase collection pipe was connected with the branch exit by a 90° elbow and packaged using an 80-mm diameter casing annulus. The other outlet of the separator was the run exit. It was an extension of the annulus casing outside the phase collection pipe and necked to 65 mm as parts of incoming fluids were extracted by the branch exit.

2.2. Working fluids

In the experiment research, the tap water and the air were applied as the liquid and the gas phase. At the experimental temperature of 20 °C, the density of water was 998.1 kg/m³ and that of air was 1.29 kg/m³. The viscosities of water and air were 1 and 0.00179 mPa.s, respectively. Therefore, the liquid–gas density ratio ξ_ρ was 774, whereas the liquid–gas viscosity ratio ξ_ν was 559.
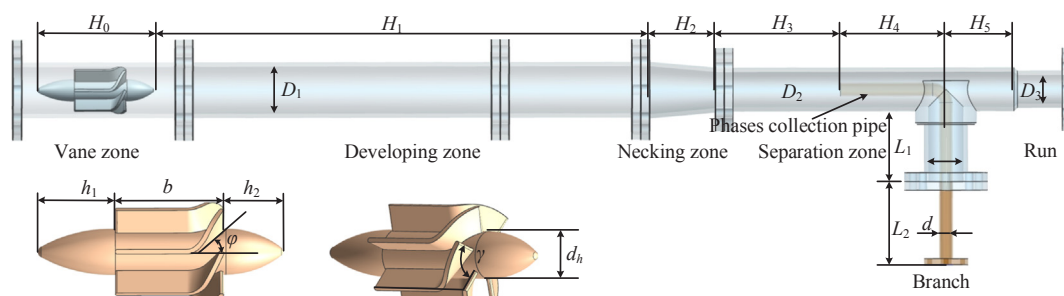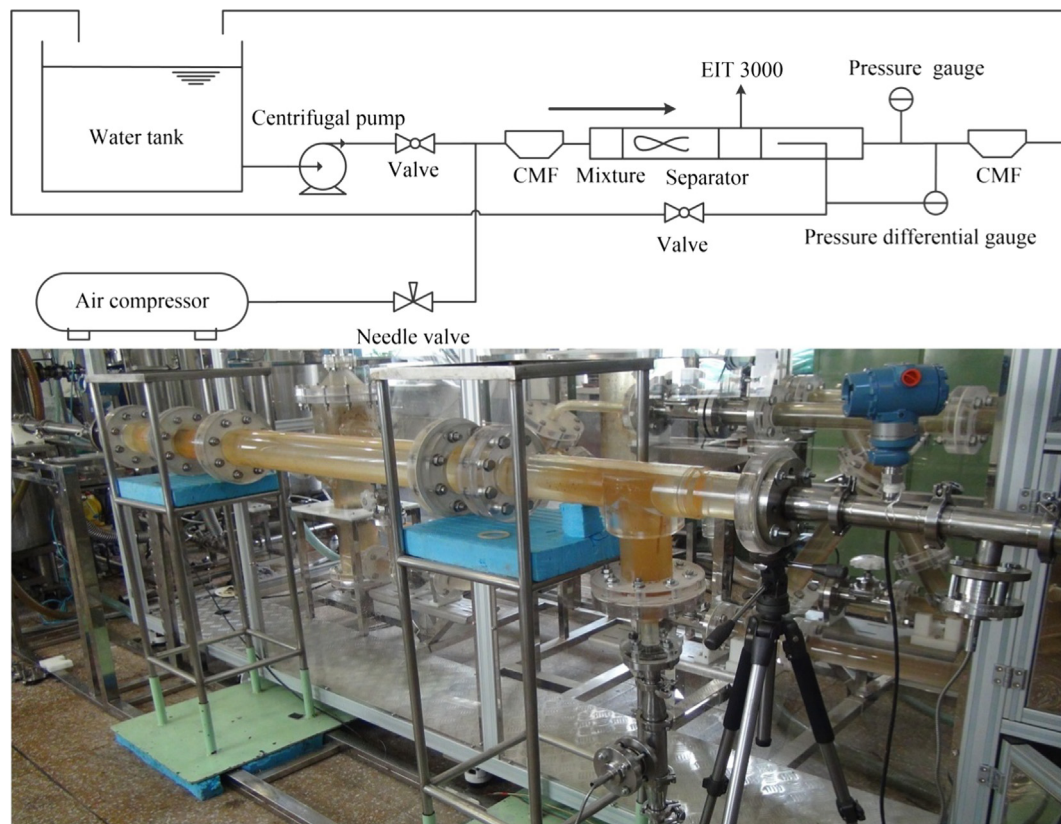

Fig. 1. The separator configuration.

Fig. 2. The experiment flow loop and the test section photograph.

2.3. Measuring technique and systematic error

A Coriolis mass flowmeter (CMF, MicroMotion F050, Emerson) was used to measure the mixture density and mass flow rate. According to literature, the maximum and minimum errors were 16.83% and −13.42%, respectively, whereas the average error was 0.82% [4].

ERT was applied for the void fraction distribution measurement in this study. Its testing components included two planes with 16 round-mounted electrodes around the pipe wall [10]. According to Wang [22], a reference error of 1% may result in up to a 10% conductivity error. Hence, the ERT should be calibrated by pure water without a gas phase prior to the experiment.

2.4. Experimental flow loop

A flow experiment was performed based on a self-circulation flow system, as shown in Fig. 2. A pressure gage for pressure measurement and an SV-5 static mixer for bubble creation were placed upstream of the separator entrance. At 0.7 m downstream of the vane zone, two groups of ERT electrodes were mounted for phase distribution measurement. Next, a pressure differential gauge was connected to the branch and run exits. Subsequently, a CMF was connected to the run exits to measure the mixture density and flow rate. In the flow loop, water from the water tank and air from the gas compressor were fully mixed, forming a bubbly dispersion flow in the static mixer; subsequently, the water flowed through the vane to induce a vortex. After the flow domain was stabilized, the gas core and water nearby entered the phase collection pipe and flowed out through the branch exits, whereas the other fluids flowed through the run pipe to enter the CMF. Finally, the two branches were discharged to a water tank. A photograph of the testing setup is shown in Fig. 2.

2.5. Operational conditions

As APG separation can be conducted on the ground, the test was conducted under atmospheric conditions. The operational conditions varied based on the inlet water flow rate, inlet air flow rate, and valve opening degree, which determined the split ratio. During the experiment, the entrance air flow rates were 1.2, 2.5, 4.0, and 6.0 m^3/h, whereas the entrance water flow rate increased from 12 to 23 m^3/h. In addition, several split ratios were used for the fixed entrance flow rate by the adjusting valve. Here, the split ratio β can be defined by Eq. (1).

$$\beta = \frac{Q_{m-branch}}{Q_{m-inlet}} \tag{1}$$

In which $Q_{m-branch}$ refers to the mixture flow rate at branch exit, while $Q_{m-inlet}$ refers to the mixture entrance flow rate. Hence, the liquid Reynolds number ranged from 42,000 to 82,000; the entrance gas volume fraction ranged from 5% to 30%; the liquid Euler number ranged from 33 to 37; whereas the split ratio ranged from 15% to 31%.

3. Numerical simulation settings

3.1. Modeling selection

The numerical simulation in this study was conducted using CFD code Fluent. The flow domain exhibited a gas–liquid two-phase swirling flow. Hence, prior to grid generation, appropriate multiphase and turbulent models should be selected.

Based on the experimental observation, a gas phase appeared in the form of bubbles at the separator entrance and then transformed into a gas core. On the basis of the studies regarding gas–liquid multiphase flows in a swirling flow field [2,23], the Eulerian multiphase model is ideal for simulating gas–liquid two phase flows. For a certain phase i, the continuity and momentum equations are as shown in Eq. (2) and Eq. (3).

$$\frac{\partial}{\partial t}(\alpha_i \rho_i) + \nabla \cdot (\alpha_i \rho_i \vec{u_i}) = 0 \tag{2}$$

$$\frac{\partial}{\partial t}(\alpha_i \rho_i \vec{u_i}) + \nabla \cdot (\alpha_i \rho_i \vec{u_i} \vec{u_i}) = -\alpha_i \nabla p + \nabla \cdot \overline{\overline{\tau_i}} + \alpha_i \rho_i \vec{g} + \sum_{i=1}^{n} K_{ji}(\vec{u_j} - \vec{u_i})$$
$$+ \alpha_i \rho_i (\vec{F_i} + \vec{F}_{lift,i} + \vec{F}_{vm,i}) \tag{3}$$

Here, i represents the ith phase; α is the volume fraction; ρ is the density; u_i is the velocity; K_{ij} represents the phase exchange coefficient, which characterizes the drag force; $\vec{F_i}$ is the body force; $\vec{F}_{lift,i}$ is the lift force; $\vec{F}_{vm,i}$ is the virtual mass force.

As with the turbulent model of continuous phase, owing to its ability in predicting anisotropic turbulence and capturing all the fluctuations of highly swirling flows bounded by curved surfaces [18], the RSM turbulent model has been applied in the simulation of swirling flow fields where the liquid phase is the continuous phase. Hence, the RSM model was applied in this study as turbulent model of continuous phase. Eq. (4) provides the equation of the RSM model.

$$\frac{\partial}{\partial t}(\rho \overline{u_i' u_j'}) + \frac{\partial}{\partial x_k}(\rho u_k \overline{u_i' u_j'}) = P_{ij} + D_{ij} + \phi_{ij} + G_{ij} - \varepsilon_{ij} + F_{ij} \tag{4}$$

Here, P_{ij} represents the stress production term, D_{ij} represents the diffusion term, φ_{ij} represents the pressure strain term, G_{ij} represents the buoyancy production term, ε_{ij} represents the dissipation term, and F_{ij} represents the production by the system rotation term.

3.2. Geometric model and grid generation

The modeling procedure was performed on the design modeler of ANSYS. A three-dimensional geometry model of the separator is shown in Fig. 3. At the vane zone, the flow domain was sliced by the space surface corresponding to the shape of the swirling blades. The location corresponding to the hub was hollow. Downstream of the gas-phase collection pipe, the flow domain was separated by the branch pipe wall.

A grid generation procedure was conducted using the ICEM CFD software platform. Considering the intricate geometrical characteristics of the fluid domain, the geometry model was separated into several parts to create a structural cell scheme with an interface as a connection between parts. For each part, the O-blocking method was used to create structural blocks. Fig. 3b shows the general cell configuration and the local details of all the cells. The cell sizes were not uniformly distributed. To consider wall friction, roughness, and possible effect of the boundary layer near the wall zone, the cells were refined with a ratio of 1.5 between adjacent cells.

3.3. Solution setting and boundary conditions

In terms of solution settings, the Eulerian multiphase model coupled with the RSM turbulent model was used in the simulation. Considering the experimental operating conditions, the primary phase in the flow domain was set as water, whereas the secondary phase in the flow domain was set as gas. The entrance bubble mean diameter from the prediction model proposed in our previous study [15] was applied as well. As the separator was mounted horizontally, gravity was set along the branch direction.

A transient simulation was reasonable considering the characteristics of gas–liquid flows. The time step size was 5 ms, and the total simulation time was 10 s. During the simulation, phase-coupled SIMPLE was applied for pressure–velocity coupling, and a second-order upwind scheme was applied for spatial discretization despite gradient being applied using the least-squares cell-based scheme. For residual settings, 10^{-6} was used to achieve a better accuracy.

In terms of boundary conditions, the velocity inlet was set for the entrance section. The water and gas phases have their own entrance velocities and phase concentrations. For the run and branch exits, outflow was selected as the boundary type. The run and branch ratios were determined from experimental measurements. For other faces in the flow domain, a stationary wall was adapted with the roughness height set according to plexiglass properties. Furthermore, a scalable wall function was applied.

3.4. Grid-independent study and effect of grid resolution on cyclone separation

Prior to any numerical simulation, a grid-independent study should first be conducted to confirm the appropriate grid scheme exhibiting sufficient accuracy with the least number of cells. Fig. 4 shows the entrance section of three grid schemes, i.e., the coarse, medium, and fine schemes with 372,064, 1,038,896, and 1,995,998 cells. To determine the simulation accuracy of each scheme, a 0.87 m/s entrance velocity and a 0.24 gas exit split ratio were used for each grid scheme. Fig. 5 presents a comparison of the radial pressure and the tangential
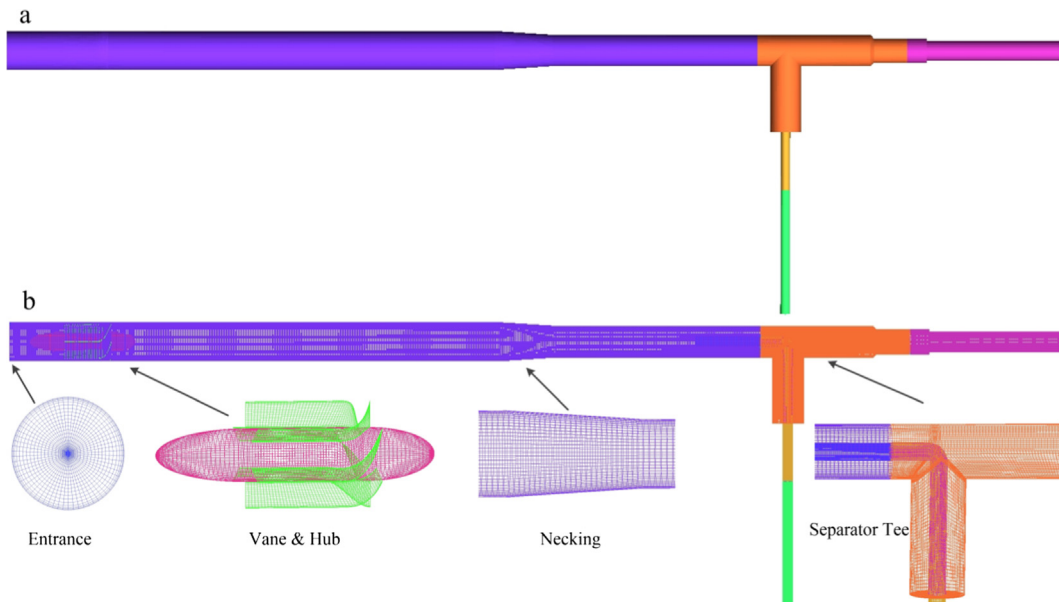

Fig. 3. Geometry model of fluid domain and mesh scheme.

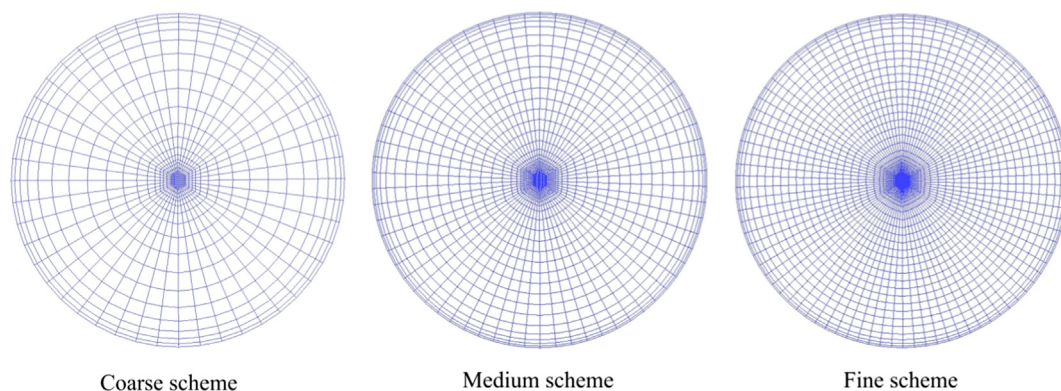Coarse scheme   Medium scheme   Fine scheme

Fig. 4. Different grid schemes.

velocity distribution 0.3 m downstream of the vane zone. It was clear that for both the pressure and tangential velocity distributions, the discrepancies between the medium and fine schemes were smaller than those between the coarse and medium schemes. The curves of the medium and fine schemes nearly coincided with each other. Hence, the medium scheme was sufficient for the simulation of the continuous phase.

Regarding the effect of grid resolution on cyclone separation, Fig. 6 shows the separation comparison of different grid schemes under fixed cases. The operating parameters were 23.1 m³/h liquid entrance flow rate, 4.0 m³/h gas entrance flow rate, and 29% split ratio. Fig. 6a shows the local void fraction 0.7 m downstream of the vane zone. It was clear that for all the grid schemes, the local maximal void fraction was 1.0 near the pipe center but remained 0 near the wall. This implied that the gas core was in the center. However, the difference in grid resolution affected the size of the void fraction curve. The divergence of the curve amplitude size between the coarse and medium schemes was significantly larger than that of the medium and fine schemes. Moreover, in terms of the separation efficiency, those of the medium and fine schemes were closer to each other than that of the coarse scheme, and the efficiencies of the medium and fine schemes were closer to the measured results. Hence, the medium grid scheme was sufficient for the gas–liquid simulation considering its accuracy and computational cost.

4. Results and discussion

4.1. Validation of numerical simulation

To validate the numerical simulation, the gas core by photographs, local void fraction by ERT and CFD, and pressure difference between the run and branch exits were compared in fixed cases. The pressure difference is the branch exit pressure minus the run exit pressure. Fig. 7

presents three cases of gas-phase distribution via numerical simulation, photographs, and ERT test result. For each case, the numerical simulation, experimental observation, and ERT test indicated the existence of a gas core in the separator. After flowing through the vane zone, the bubble dispersion formed a gas core rapidly. Subsequently, the gas core flowed into the phase collection pipe. Owing to the pressure difference between the branch and run pipes, a gas core with possible liquids nearby flowed out of the branch exit. For each case, the gas phase distribution from the numerical simulation corresponded well with the experimental observation in terms of both tendency and gas core width. Discrepancy primarily occurred at the gas–liquid interface, as measured by ERT, it was wider than those from the photographs and simulation results. This was owing to the resolution of the ERT pixel. As described in Section 2.3, 16 electrodes were mounted around the pipe wall, and the concentration reconstruction matrix contained 20 pixels evenly distributed at a radial length of 100 mm. Moreover, as the mixture conductivity changed abruptly from minimal to maximal at the gas–liquid interface, the gradient measured might be smaller than it really was owing to the pixel resolution. More than 1 pixel was required for the conductivity transition, thereby inducing a size discrepancy at the gas–liquid interface [24,15]. However, the total measurement was not affected significantly as the measured gas core region size was similar to the photograph and simulation results. The void fraction in the gas core zone was 100%.

To further validate the numerical simulation, Table 2 provides a comparison of pressure difference between the branch and run exits. The absolute pressure at the entrance, the branch, and the run exit were reported as well. In all cases, the simulation results were similar with the measurements from the pressure gauge. Moreover, it was clear that the simulated pressure difference was slightly smaller than that of measured. This may be caused by the simplification during the modeling, in which the blades were regarded as a surface without thickness.
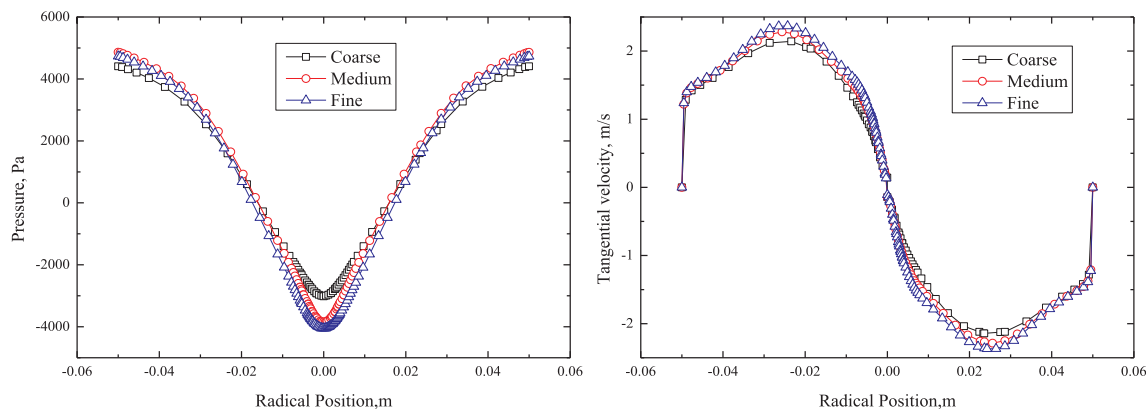

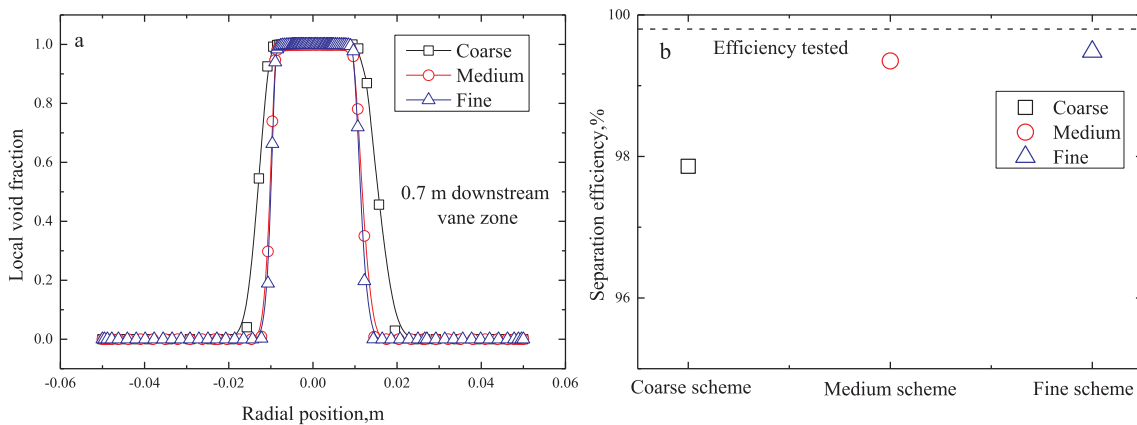**Fig. 5.** The radial pressure and the tangential velocity distribution 0.3 m downstream the vane zone.

Fig. 6. Influence of the grid resolution on the separation performance.

Cai [3] discovered similar trends between the CFD and measured results.

4.2. Phase distribution in separator

As shown in Fig. 7, the gas core size is sensitive to the entrance flow rate. Comparing the numerical validation of Cases 1 and 2, it was clear that as the gas entrance flow rate increased, the gas core widened. Comparing the numerical validation of Cases 1 and 3, it was clear that as water entrance flow rate decreased, the gas core size increased as

well. This can be attributed to the section void fraction and pressure distribution, which will be discussed in the next subsection. As the gas entrance flow rate increased, the section water volume fraction decreased, resulting in a lower pressure drop from the wall to the pipe center, as shown in Fig. 8a, owing to the density variance in the liquid and gas. Consequently, the section void fraction increased more significantly and the gas core size increased. When the entrance gas flow rate was fixed and the entrance liquid flow rate decreased, the section void fraction increased and the pressure drop was less owing to the smaller liquid phase, causing the gas core to widen.
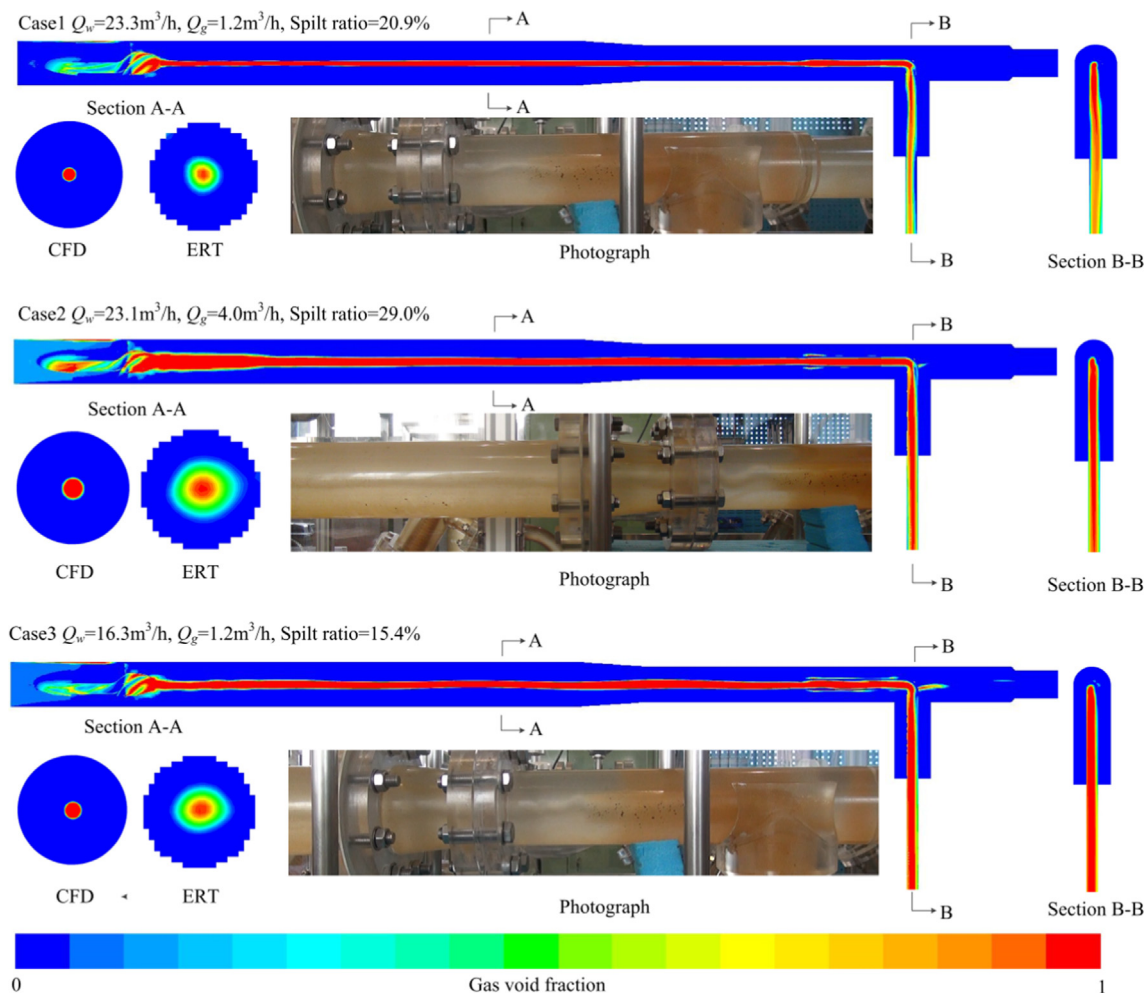

Fig. 7. Comparison between the numerical simulation and the experiment measurement under various operating conditions.

Table 2

Operating condition parameter for numerical validation cases.

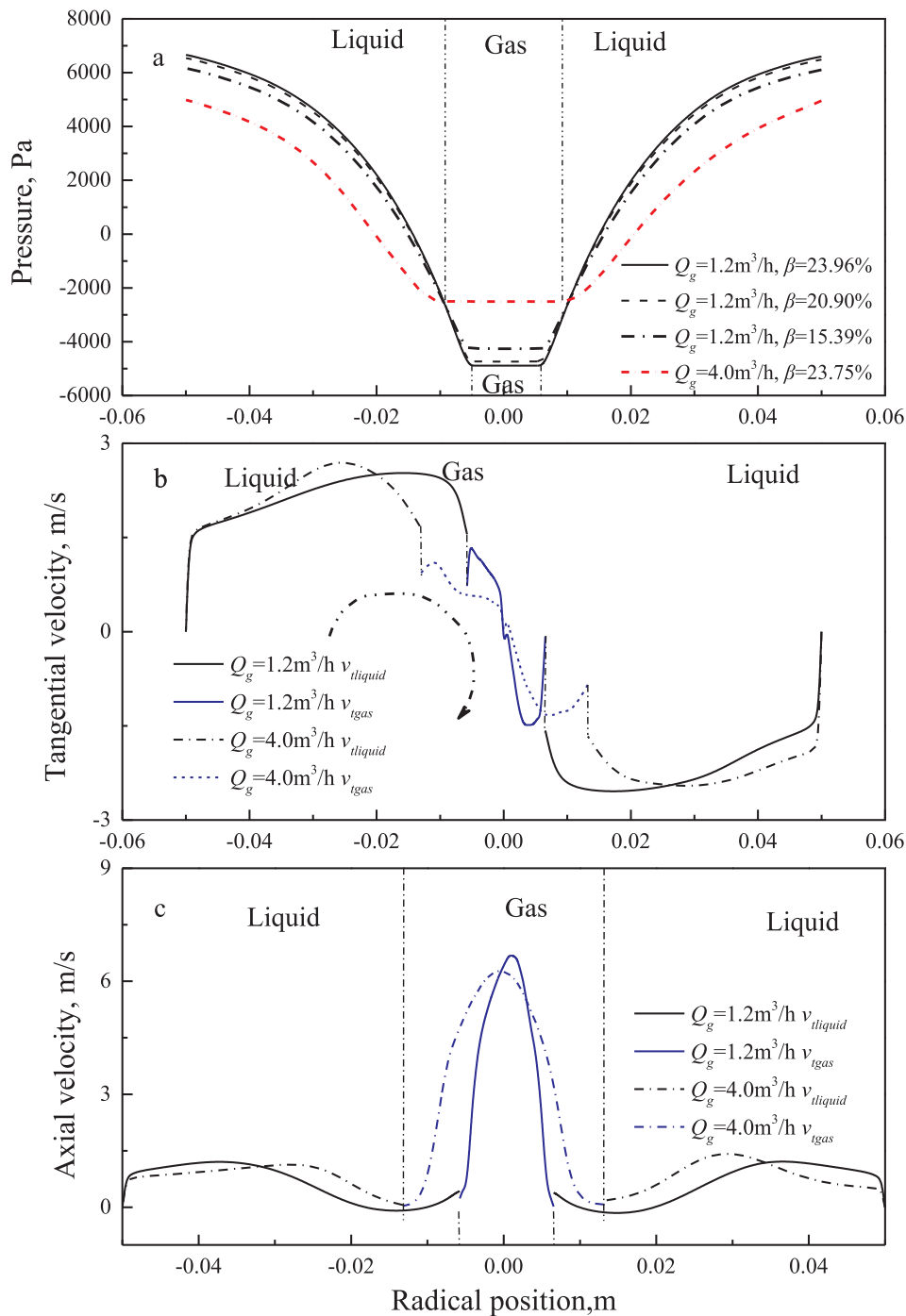| Case No.	Case parameter						Branch- run pressure difference (kPa)	
	Liquid entrance flowrate (m³/h)	Gas entrance flowrate (m³/h)	Split ratio, %	Pressure (kPa)				
				Inlet	Branch	Run	Experiment result	Simulation result
1	23.3	1.2	20.9	89.25	64.71	76.48	−13.06	−11.77
2	23.1	4.0	29.0	123.05	91.84	107.40	−16.35	−15.56
3	16.3	1.2	15.4	53.63	40.90	44.63	−4.68	−3.73

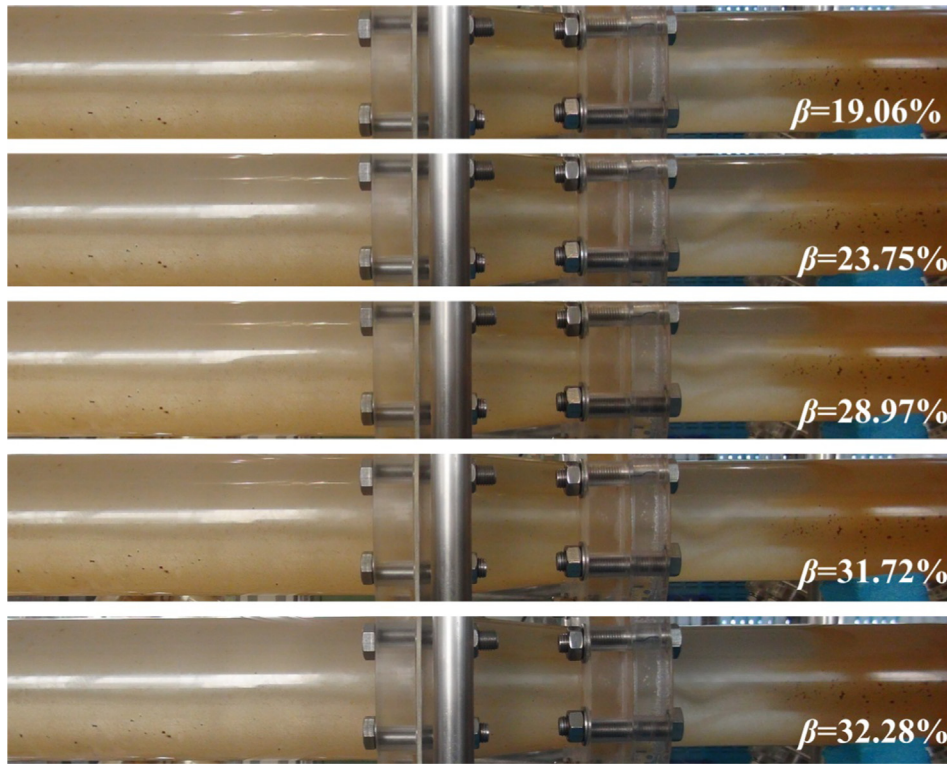**Fig. 8.** The radial pressure and the velocity distribution 0.3 m downstream vane zone.

Fig. 9. The gas core distributions under various split ratios when $Q_l = 23$ m^3/h, $Q_g = 4.0$ m^3/s.

The split ratio effect is apparent when fixing the entrance flow rate. Fig. 9 shows the gas core size variance as the split ratio increased from 19.06% to 32.28% under experimental observations. It was clear that the gas core became narrower as the split ratio increased. This trend is more apparent in the numerical simulation results shown in Fig. 10a, where the local void fraction curve narrowed down as the split ratio increased at 1.2 m downstream of the vane zone. The phenomenon can be explained in terms of sectional pressure distribution changes. As shown in Fig. 8a, for a 1.2-m^3/h gas entrance flow rate, when the split ratio increased, less fluid remained in the run pipe, and the velocity in the run exit decreased. This resulted in a larger pressure drop near the wall in the swirling flow field, rendering a larger slope of the pressure curve in Fig. 8a. The gas core was sensitive to the operating parameters including the entrance flow rate and split ratio.

4.3. Velocity distribution in the separator

Fig. 11 shows the pathlines inside the separator under different gas entrance flow rates when the liquid entrance flow rate was approximately 23 m^3/h and the split ratio was approximately 24%. For a fixed gas entrance flow rate, the liquid pathlines and gas pathlines are presented separately. For the liquid phase, the pathlines twisted and rotated inside the separator downstream of the vane zone. When the liquid phase coincided with the branch annulus, the situation was similar with a flow in a tee, where parts of the liquid phase filled the annulus in the branch, and a small part flowed through the branch exits with the gas phase. The remaining liquid flowed from the separator through the run exit. When the gas entrance flow rate increased from 1.2 to 4.0 m^3/h, the trend of the pathline wrapping degree was more apparent for the developing section downstream the vane zone and upstream of the separation zone. As with the gas phase, the pathlines were not straight but slightly inclined upside compared with that of the water phase upstream the vane zone. This can be attributed to the phase density variance and gravity. The gas phase density was almost 0.1% of the liquid phase. As the gravity acceleration was along the branch exits, the gas transferred in the opposite direction by buoyancy effects in short distances.

For analysis convenience, the gas velocity and liquid velocity are summarized in an entire curve under fixed gas entrance flow rate conditions, as shown in Figs. 8 and 10, respectively. Several trends are shown in the two figures. The first trend relates to the symmetry of the velocity curve. To include the effect of gravity on the horizontally mounted separator, the velocity curve was sampled in a horizontal line crossing the pipe center. The rotation direction was clockwise, as shown in Fig. 8b. At a section 0.3 m downstream of the vane zone, the tangential velocity of the gas phase exhibited asymmetry near the interface with the liquid. At 1.2 m downstream of the vane zone, the asymmetry was slight. After vortex was fully developed in the swirling flow field, the effect of gravity was slight. The second trend was pertaining to the gas–liquid interface. In the tangential motion, velocity slip existed in the gas–liquid interface. This is attributed to the discontinuity of the phases. The third trend was pertaining to the gas–liquid volume fraction. As the gas entrance flow rate increased, the gas core widened. As shown in Fig. 8c, in the developing section, the liquid phase moved away from the pipe center, whereas the radial tangential velocity maximal location moved toward the wall. The same phenomenon was observed in the separation section, as shown in Fig. 10c.

4.4. Swirling intensity distribution in the separator

Based on the phase and velocity distributions above, the swirling intensity is analyzed in this subsection. The gas–liquid two phase swirling number is proposed based on our previous study. Eq. (5) expresses the gas–liquid two phase swirling intensity, which is the ratio of the axial flux of the tangential momentum to the axial flux of the axial momentum [14].

$$\Omega = \frac{1}{r_2} \frac{\int_{r_1}^{r_2} \alpha_l \rho_l r^2 u_{lt} u_{lx} + \alpha_g \rho_g r^2 u_{gt} u_{gx} dr}{\int_{r_1}^{r_2} \alpha_l \rho_l r u_{lx}^2 + \alpha_g \rho_g r u_{gx}^2 dr} \tag{5}$$

In which, ρ is the density; subscript l refers to the liquid-phase parameter; g refers to the gas-phase parameter; u_t refers to tangential
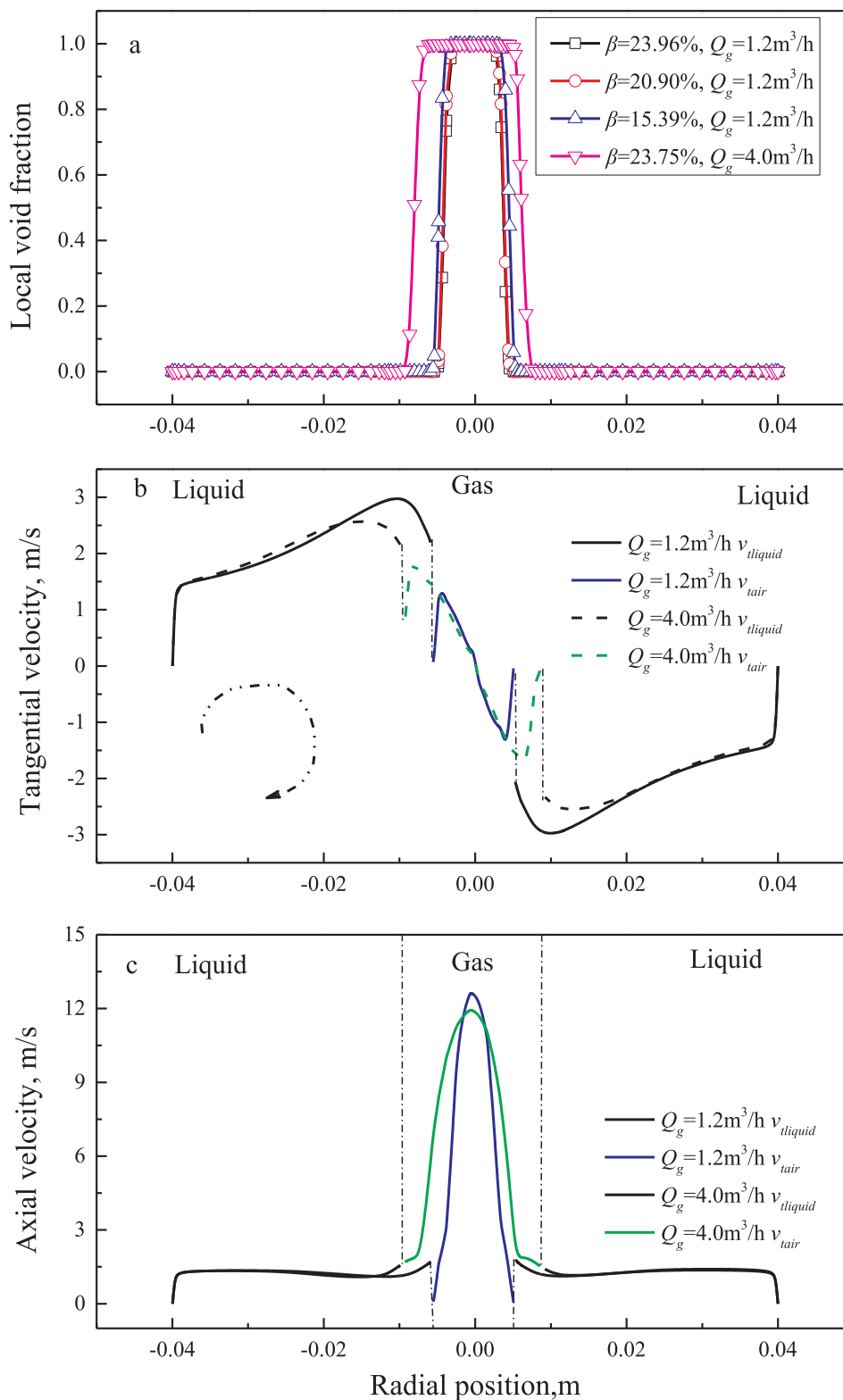
Fig. 10. Radial phase and velocity distribution 1.2 m downstream vane zone.

velocity; whereas u_x refers to the axial velocity.

As shown in Fig. 12a, the entrance flow rate was 1.2 m³/h, and the split ratio increased from 15.39% to 23.96%. Downstream of the vane zone, the swirling number increased in a short distance and subsequently suffered from a small valley. This was because the hub downstream of the vane zone affected the overcurrent area. As the gas core was narrow, when the overcurrent area increased, the centroid of the liquid phase approached the pipe center, which reduced the tangential momentum, thereby promoting the appearance of small valleys downstream the vane zone. Subsequently, under the effect of inertia, the swirling intensity continued to increase and then began attenuating until necking occurred in the influential section. In the necking influential section, the axial momentum decreased faster than the section tangential momentum owing to the acceleration of the necking
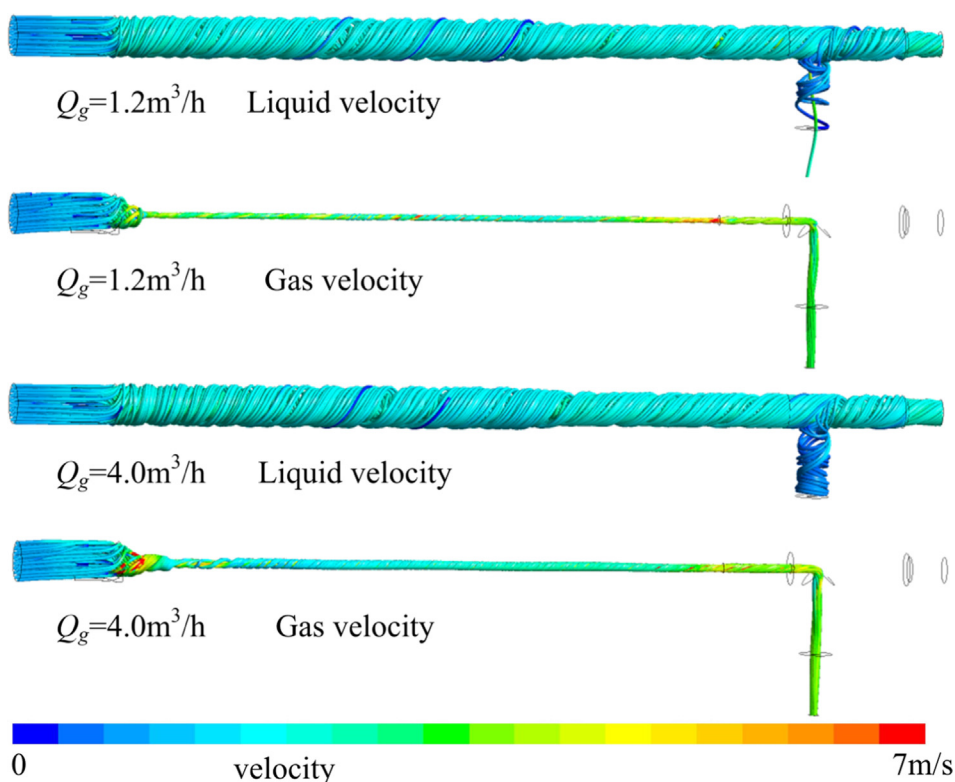
Fig. 11. The pathlines under various gas entrance flow rates when the liquid entrance flow rate is fixed around 23 m^3/h and the split ratio is fixed around 24%.

downstream, which resulted in an increase in the swirling number. When entering the first necking, the axial velocity increased, whereas the liquid centroid moved toward the pipe center, causing an abrupt decrease in the swirling intensity. After entering into separation zone, the swirling number decreased abruptly again when the entrance of the phase collection pipe appeared. In this section, owing to the flow in the phase collection pipe increasing the total axial section velocity and decreasing the total section tangential velocity, the swirling number decreased. However, owing to the abrupt necking, the swirling number increased again in the second necking influential section. As the split ratio increased, the flow rate in the run branch decreased, and the pressure near the pipe wall increased in the axial section, causing the gas core size to decrease. Consequently, the liquid centroid in the section moved toward the pipe center, thereby decreasing the tangential momentum. Meanwhile, the axial momentum decreased faster than the tangential momentum as more axial momentum components "disappeared" from the elbow to the branch exits. In other words, the liquid-phase outside collection pipe was the main component providing tangential momentum, whereas the liquid in the phase-collection pipe provided an equivalent or a more significant axial momentum component. Hence, the swirling intensity will increase with the split ratio owing to the decrease in axial momentum in the swirling flow field center.

Fig. 12b shows the swirling intensity curves with different split ratios along the separator when the gas entrance flow rate was 4.0 m^3/h. The general trend was similar with that of 1.2–m^3/h inlet gas flow rate conditions. A difference was observed in the developing section immediately downstream of the vane zone. As the gas entrance flow rate increased, the swirling number increased to beyond 1.6 instead of exhibiting a minor valley. This is reasonable based on the analysis of the gas–phase distribution shown in Fig. 7. Under a 4.0–m^3/h gas entrance flow rate condition, the gas phase occupied a considerable volume of the pipe center in the developing section, pushing the liquid phase toward the pipe wall. The liquid phase tangential velocity was large and produced more tangential momentum as the liquid centroid was closer

to the pipe wall. Meanwhile, owing to density difference, a larger gas phase appeared and resulted in less axial momentum. Hence, the swirling number increased continuously compared with that of the 1.2–m^3/h gas entrance flow rate condition.

By understanding the variation regulars of the swirling number, it becomes possible to illustrate the method to optimize the separator. The degassing procedure can be regarded as collecting the gas phase at an appropriate Ω range. Consequently, it's possible to adjust the geometry parameters to control the Ω curve so as to optimize the separator. Appropriate adjustment of the Ω curve pertains to initial value and z/D range accordingly. In Fig. 12 the initial value of the swirling numbers were nearly the same for all the cases. According to Yin et al. [26], initial swirl intensity S was sensitive to the blade geometry parameters φ and d_h in regardless of the fluid velocity. Increasing these parameters resulted in a larger S accompanied with a larger pressure drop [3]. Therefore, the balance between the initial swirl intensity and the pressure drop should be attempt first for separator optimization. Furthermore, axial range of the Ω curve could be determined by the distance between the vane zone and the phase collection pipe. An extremely small distance where the Ω is too large may interrupt the stable operation of the gas core. Meanwhile, an extremely large distance where the Ω is too small may induce gas core disruption. In addition, necking can enhance the Ω in upstream section. Consequently, adjusting the location of the phase collection pipe and the necking upon the swirling intensity variance by the simulation or experiment could assist the optimization of the separator.

4.5. Separation performance study

Fig. 13 shows the variation of the separation efficiency with the split ratio under various phase entrance flow rates. At a fixed phase entrance flow rate, the separation efficiency increased with the split ratio. When the split ratio exceeded a certain value, the separation efficiency remained at approximately 100% without decreasing, which was reasonable. The separation efficiency was sensitive to the relative locations
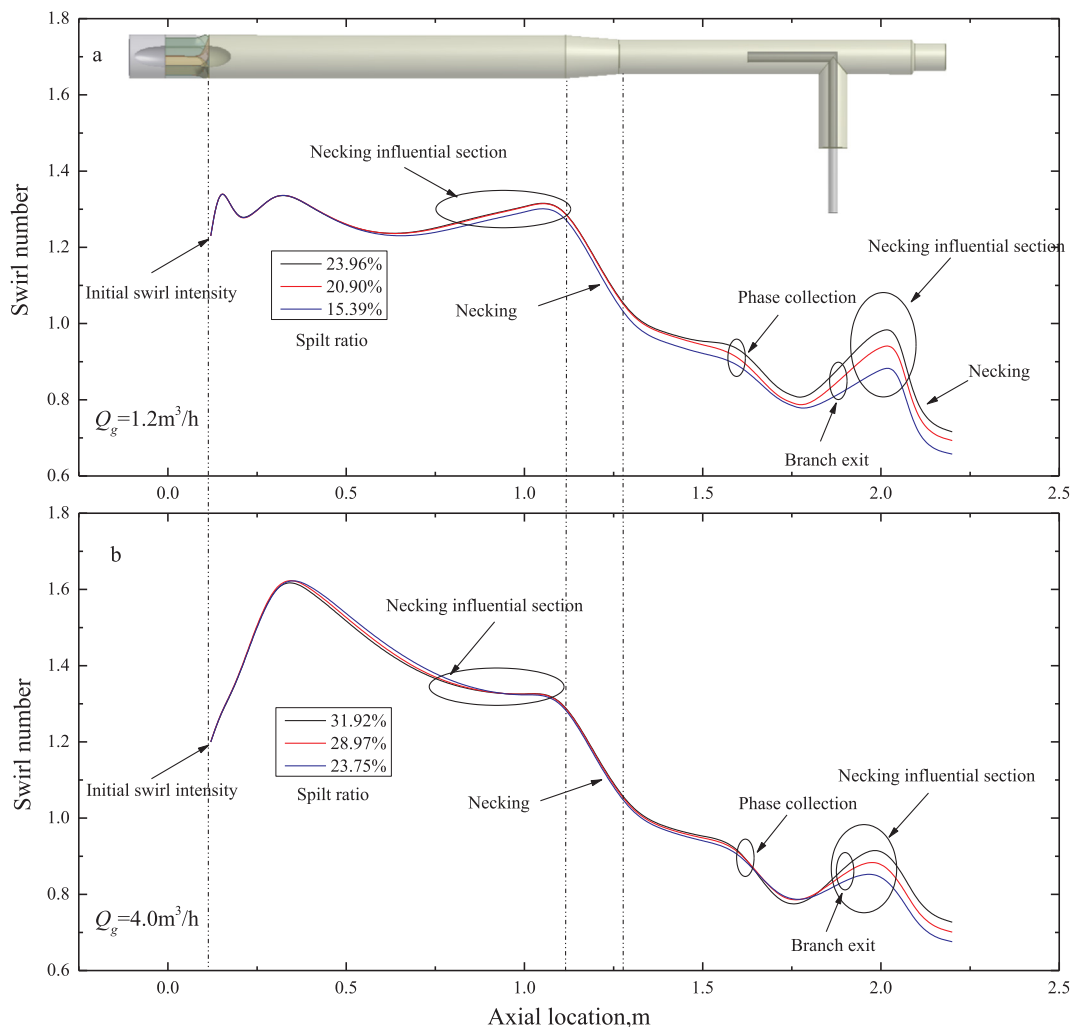
Fig. 12. The gas–liquid swirling number variation along the pipe axis under various operating conditions.

of the gas–liquid interface and split flow face, which will be discussed in the next subsection. Under fixed phase entrance flow rates, the gas core size decreased when the split ratio increased. A critical split ratio existed for which the gas–liquid interface was nearly coincident with the split flow face. As the split ratio was larger than the critical split ratio, the gas core that was fully located in the volume was surrounded by the split flow face. Hence, the separation efficiency remained at

approximately 100%.

As the entrance phase flow rate changed, the split ratio required to achieve a separation efficiency of approximately 100% differed. As shown in Fig. 13, as $Q_g = 2.5$ m^3/h, the split ratio required to achieve a separation efficiency of approximately 100% decreased when Q_l was larger. The same was observed for $Q_g = 6.0$ m^3/h. To analyze this phenomenon systematically, we defined a critical split ratio β_c, which
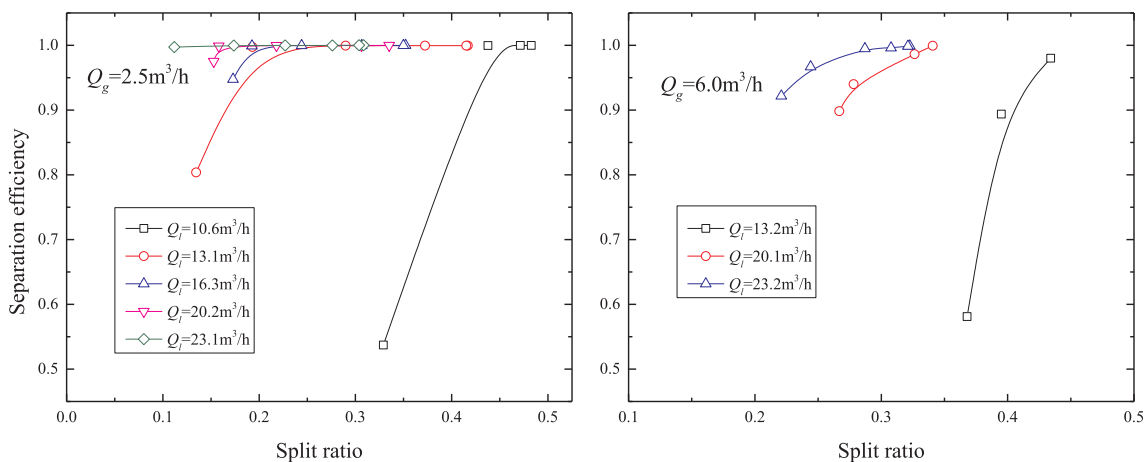

Fig. 13. Influence of the split ratio on the separation efficiency under fixed entrance flow rate.
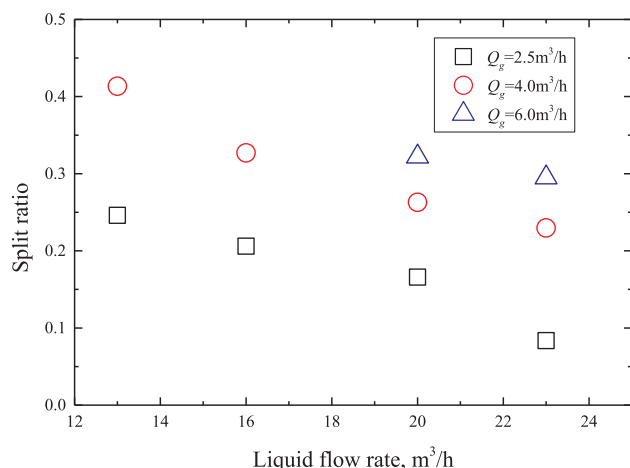
Fig. 14. The critical split ratios under various entrance flow rates.

implies that for a fixed entrance phase flow rate condition, the separation efficiency is 99.5%. Fig. 14 summarizes the β_c of different phase entrance flow rate conditions. As shown, for a fixed gas entrance flow rate, β_c decreased when the liquid entrance flow rate increased, which was reasonable. As the liquid entrance flow rate increased, the pressure drop in the separator increased, resulting in a higher pressure away from the pipe center in the axial section. This pushed the gas–liquid interface moving to the pipe center and resulted in a thinner gas core. A smaller split ratio was required such that the gas–liquid interface was nearly coincident with the split flow face. Hence, β_c decreased. As the liquid entrance flow rate was fixed and the gas entrance flow rate increased, the opposite mechanism applied. A larger split ratio was required to push the gas–liquid interface to coincide with the split flow face. Hence, β_c increased.

In general, the separation efficiency was affected by the gas core size. The operating parameters, including the split ratio and phase entrance flow rate affected the gas core. Hence, these parameters affected the separation efficiency. Appropriate adjustments of the valve opening degree at the run exit or the phase entrance flow rate can enhance the separation efficiency. When the split ratio exceeded the critical split ratio and continued to increase, although almost all the gas phases can be collected by the branch exit, a larger amount of the water phase was involved, thereby affecting the separation performances. Hence, a dimensionless parameter should be introduced to evaluate the water in the phase collection pipe. Yin et al. [26] introduced the entrainment ratio λ to characterize the liquid phase. It can be expressed as shown in Eq. (6), which implies that the liquid phase in the branch exit should be small in terms of economic optimization.

$$\lambda = \frac{Q_l - Q_{l-run}}{Q_l} \tag{6}$$

As shown in Fig. 15, under fixed entrance gas and liquid flow rates, the water entrainment ratio increased as more mixture bypassed the branch exit, and the curves were approximately a sloped line. Hence, once the split ratio exceeded the critical split ratio, the gas separation achieved a limit, whereas a larger amount of liquid phase would be collected if the split ratio continued to increase. Hence, the critical split ratio can be regarded as the optimal split ratio. As shown in the figure, at a fixed split ratio, the water entrainment ratio increased with the liquid entrance flow rate. This is because, as the liquid flow rate increased, the gas core size decreased, and more liquid phase moved into zones surrounded by the split flow face. Meanwhile, when the gas entrance flow rate increased, a smaller liquid phase existed in the zones surrounded by the split flow face, which would flow pass the branch exit.

4.6. Separation mechanism and variation with operating parameters

Based on the discussion above, the separation mechanism is proposed in this subsection. The sections shown in Fig. 16 are axial sections. The separation behavior is discussed based on the relative locations of two faces, namely the gas–liquid interface and the split flow face. In the swirling flow field, gas gathers in a continuous phase. The gas core diameter is determined by the dynamic equilibrium of the pressure and the centrifugal force in radial direction. As both the annulus flow and gas core have their own pressures, the latter counteract and yield a net pressure at the interface, which can be called the pressure difference as well. When the equilibrium of relative pressure and centrifugal force are disturbed, a new equilibrium will be achieved and hence the location of phase interface will shift. Meanwhile, the split flow face is an interface inside which fluids will bypass a separator through the branch exit. Whereas the fluid outside the split flow face will bypass the separator through the run exit. The distribution of the split flow face is determined by the split flow rate. Subsequently, when the gas–liquid interface is inside the split flow face, the gas phase can be collected by the phase collection pipe. On the contrary, when the gas–liquid interface is outside the spilt flow face, only a part of the gas can be collected through the branch exit with the remaining gas phase bypassing the run exit.

Theoretically, when the gas–liquid interface is coincident with the split flow phase, 100% of the gas will be separated with little water phase collected in the branch exit. However, the gas–liquid flow instantaneous disturbance, thickness of phase collection pipe, and tangential phase slippage cause disturbance and minor discrepancies to the mechanical model. Nonetheless, the model can provide an ideal explanation of the separation mechanism under various operating conditions as the separation procedure is only sensitive to the entrance gas
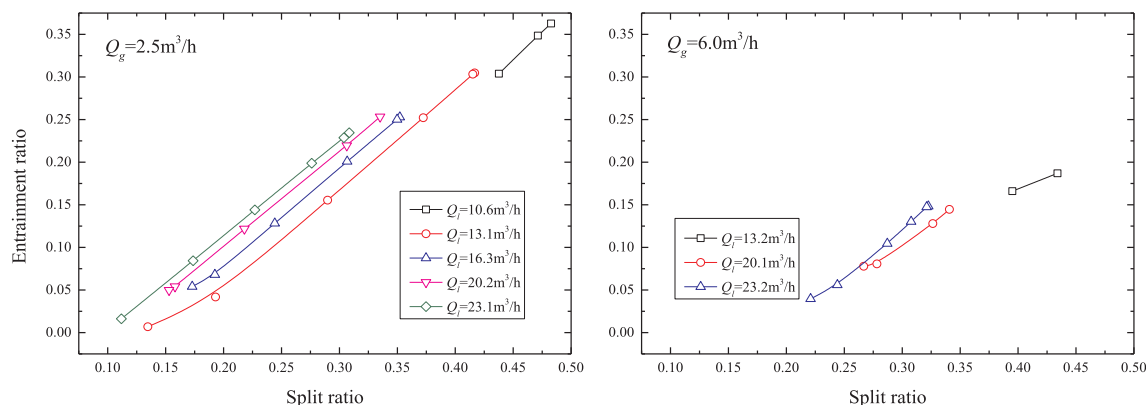

Fig. 15. Influence of the split ratio on the entrainment ratio under fixed entrance flow rate.
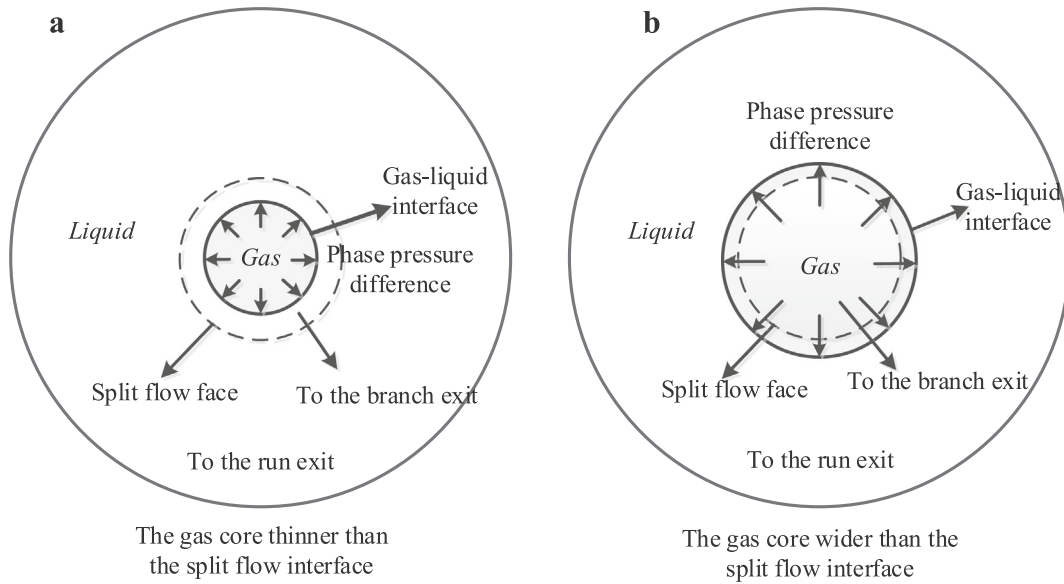
Fig. 16. The gas–liquid separation mechanism.

volume fraction and the pressure difference of exits. The material variation and the higher pressures may bring a different liquid–gas density ratio ξ_ρ and liquid–gas viscosity ratio ξ_ν. Moreover, in much higher pressures, part of the dissolved gas may desorb [25] to increase the gas void fraction. Nevertheless, once the fluid inside the separator is the swirling annulus flow [16], the mechanism model is still applicable. A critical split ratio still exists to achieve a separation efficiency of approximately 100%.

The separation mechanism is closely sensitive to the split ratio. As shown in Fig. 17a, when the split ratio was smaller than 0.25, both the separation efficiency and entrainment ratio increased with the split ratio. This corresponds with Fig. 16b, in which the gas–liquid interface was outside the split flow face. As the spilt ratio increased, the split flow face enlarged consequently. At the same time, the pressure inside split flow face decreased as more fluids flowed by. This breaks the former pressure difference-centrifugal force equilibrium, rendering the centrifugal force stronger than the pressure difference at the interface. Therefore, the gas core radius will decrease to slash the centrifugal force and rebuild the force balance. Consequently, more gas arrived at the branch exits when the split ratio increased. The entrainment ratio of water originated from the disturbance arising from phase slippage and other factors discussed in the last paragraph. When the split ratio was larger than 0.25, the separation efficiency stopped increasing, whereas the entrainment ratio continued to increase with the split ratio. This

condition corresponds with Fig. 16a, in which the gas core was fully located inside the volume enclosed by the split flow face. Under this condition, the gas was fully collected by the phase collection pipe. When the split ratio continued to increase, the gas core size reduced, and more water phase moved into the zone enclosed by the split flow face. This resulted in a larger water entrainment ratio which is not beneficial for degassing liquids.

Fig. 17a and b together show how the entrance operating parameters affect the separation mechanism. Although β_c was the threshold of the two separation mechanism models, it changed by the varying entrance condition. Based on the discussion of swirling intensity in Section 4.4 and the separation mechanism model, the gas core size significantly affected the separation. The gas core size was affected by the entrance gas volume fraction, which was determined by the phase entrance flow rates. Therefore, changes in the phase entrance flow rates yielded various critical spilt ratios. A larger entrance gas volume fraction required a higher β_c to enable a split flow face package gas–liquid interface and achieve a separation efficiency approximate to 100%.

4.7. Relationships among operational parameters

After investigating the separation efficiency, the relationships among the operational conditions should be investigated for use in further industrial applications. In this study, the operational parameters
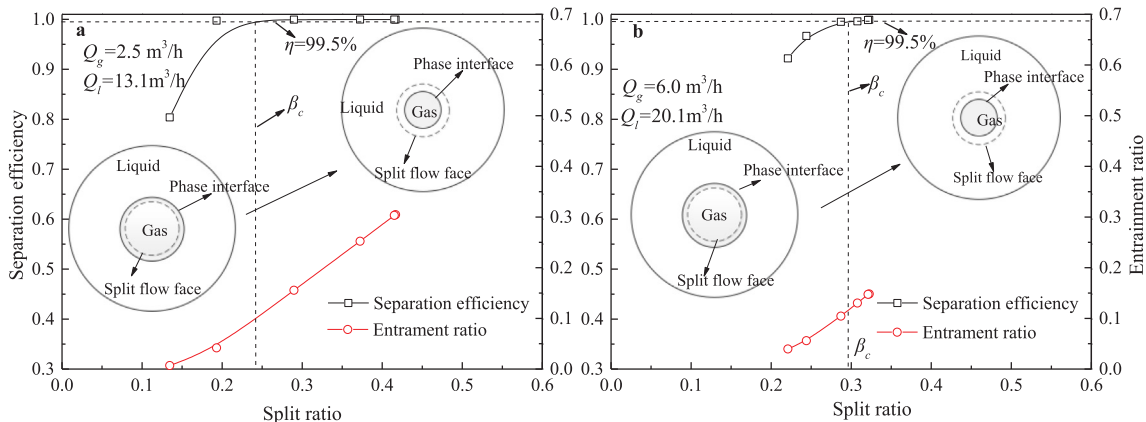

Fig. 17. The separation mechanism transition with variation of the operating parameters.
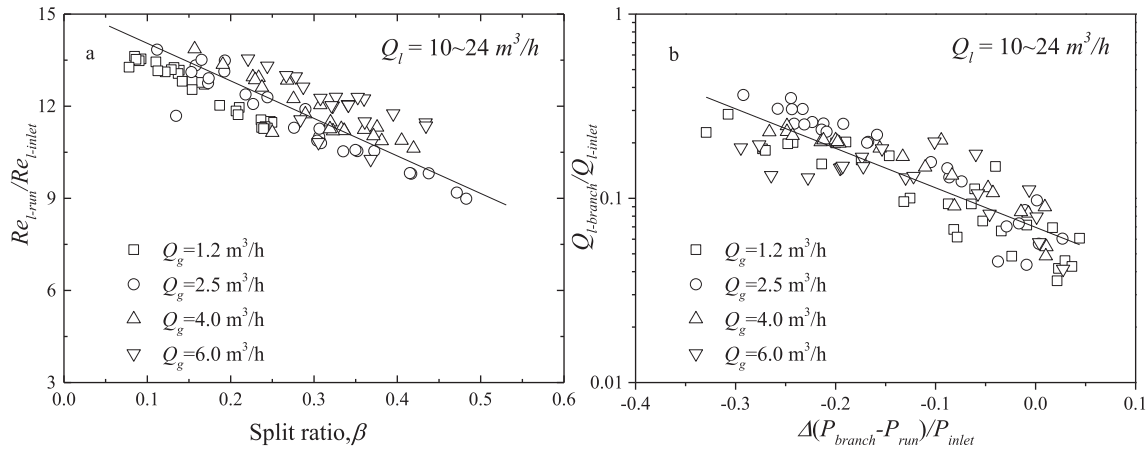
Fig. 18. Relationships for the operating parameters (a. $Re_{l-inlet}/Re_{l-branch}$ vs. Split ratio, b $Q_{l-branch}/Q_{l-inlet}$ vs. pressure difference.)

were the liquid flow rate at the overflow, pressure difference between the branch and run exits, and the split ratio.

Fig. 18a shows the relationship between the dimensionless run exit liquid flow rate and the split ratio, where Re_{l-run} and $Re_{l-inlet}$ are the liquid phase Re of the entrance and run exits, as defined in Eq. (7) and Eq. (8) as follows:

$$Re_{l-inlet} = \frac{4\rho_l Q_{l\text{-}run}}{\pi\mu_l D_e} \tag{7}$$

$$Re_{l-run} = \frac{4\rho_l Q_{l-run}}{\pi\mu_l D_r}, \tag{8}$$

where ρ_l and μ_l are the density and viscosity of water, respectively. Subsequently, $Re_{l-run}/Re_{l-inlet}$ is proportional to $Q_{l-run}/Q_{l-inlet}$. As the gas phase is a minority at the run exit, the liquid phase can be regarded as the main component of the residual mixture flow rate despite being collected by the branch. Hence, the approximate linear relationship between $Re_{l-run}/Re_{l-inlet}$ and the split ratio as well as the slope were negative, signifying that a larger split ratio results in less liquid-phase flow bypassing the run exit. The regression variation originated from the effect of the gas phase. As the split ratio was significantly lower than the critical value, the gas phase might appear in the run exit, causing discrepancies in the plot. As the entrance gas phase concentration increased, although the split ratio increased, a discrepancy was observed in the line curve because the split ratio was defined by the mixture flow rate, whereas $Re_{l-run}/Re_{l-inlet}$ was pertaining to the liquid phase only.

Regarding the relationship between the liquid flow rate at the branch exit and the pressure exit difference, the dimensionless data are plotted in Fig. 18b. As shown in logarithmic coordinate system, as the run exit pressure became gradually lower than that of the branch exit, the liquid flow rate at the branch exit decreased, which was reasonable. When the pressure difference between the branch and run exits increased, the run exit pressure decreased, and the branch exit pressure increased. The pressure drop between the entrance and run exit increased. In the axial section, the pressure away from the pipe center was closely related to the run exit, whereas the pressure near the pipe center was closely related to the branch exit pressure as the pipe center fluid domain was connected to the branch exits. When the pressure difference increased, the gas-side pressure increased and liquid-side pressure decreased at the gas–liquid interface. The interface moved toward the wall side and the gas core widened. A smaller percentage of entrance liquid phase flowed pass the branch exit through the split flow face.

Another noteworthy relationship is that between the pressure difference and split ratio, which directly affects the operation and hence the downstream separation performance. In each case of Fig. 19, a linear relationship can be regressed. The branch exit pressure became much lower than that of the run exit as the split ratio increased. Based

on the separation mechanism above, as more fluid mixture flowed into zone packaged by the split flow face, the pressure in this zone will decrease accordingly. Whereas the pressure difference out and in of the split flow face will increase. As the zone outside the split flow face was connected to the run exit and the zone inside was connected to the branch exit. As such, pressure can be transmitted. Hence, the pressure difference decreased with the split ratio increase.

5. Conclusion

Based on APG separation from produced fluids, a thorough investigation including the separation performance, the separation mechanism, the influential operating parameters, and their relationships on a vane-type degassing separator was conducted in this study. An ERT and a CMF were used in the flow experiment for phase distribution and mixture density measurements, respectively. The Eulerian multiphase model coupled with the RSM turbulent model was applied to simulate the fluid domain inside the separator. The conclusions are as follows:

Through application of two-phase swirling number, the swirling intensity variation in the whole separator was discussed. The mechanism of the operating parameter and the separator configuration affect the swirling intensity was analyzed. Then the optimization method was proposed on the basis of the swirling number variation inside the separator. Subsequently, the separation performance and its influential factors were investigated. Results showed that as the split ratio was smaller than critical value β_c, the separation efficiency increased with the split ratio. As the split ratio was larger than β_c and increased continuously, the separation efficiency achieved approximately 100% with a larger liquid phase in the branch exit. β_c can be regarded as the optimal split ratio. It increased with the entrance gas flow rate and decreased as the entrance liquid flow rate increased.

A gas–liquid separation mechanism model was proposed with definition of the split flow face. The relative location of the gas–liquid interface and the split flow face determined the efficiency that the gas phase was separated. The entrance gas volume fraction and the pressure difference between the exits affect the separation performance by the change in the relative locations of the gas–liquid interface and the split flow face. Finally, the relationships among the operating parameters were studied. $Re_{l-run}/Re_{l-inlet}$ exhibited a linear correlation with the split ratio as did the dimensionless pressure difference between the branch and run exits. A linear relationship in the logarithmic coordinate was exhibited between the liquid flow rates at the branch exit and the split ratio.

The data in this work can provide reference to the system sharing the similar phase density ratio and phase viscosity ratio. The mechanism model proposed is applicable for annulus swirling flow under various pressures. All these are beneficial to further design and
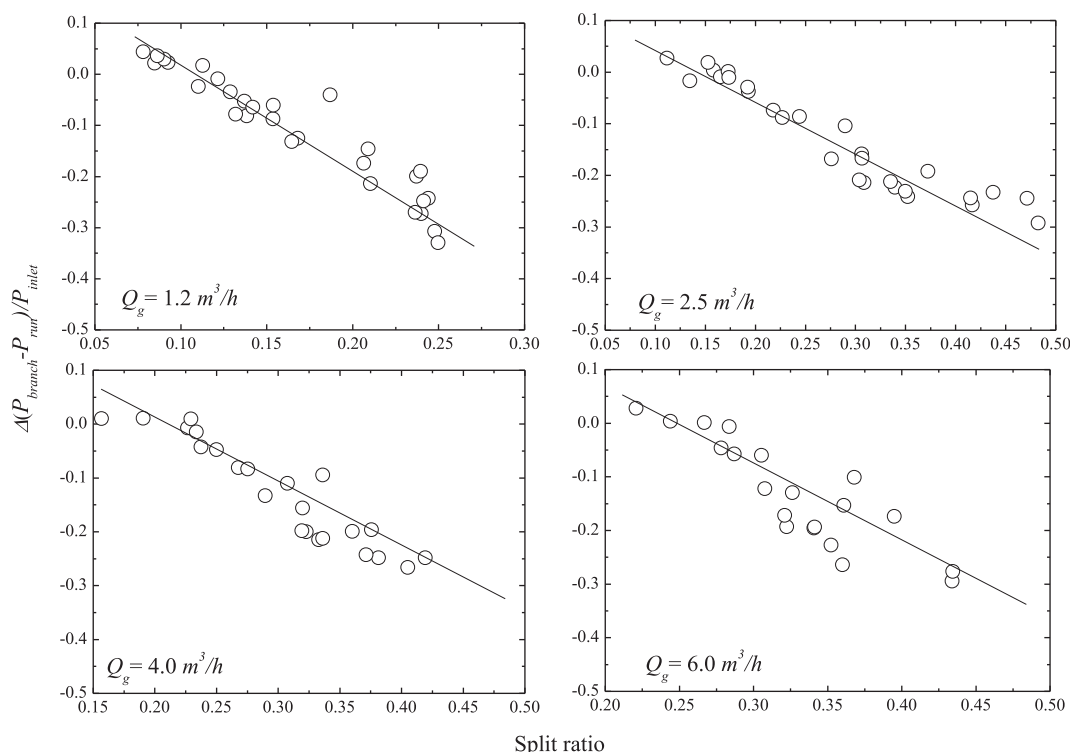
Fig. 19. The pressure difference between the branch exit and the run exit vs. the split ratio under various operating conditions.

optimization of the vane-type separator under various entrance conditions.

CRediT authorship contribution statement

Shuo Liu: Investigation, Methodology, Writing - original draft. **Jian Zhang:** Project administration, Data curation. **Li-song Wang:** Visualization, Software. **Jing-yu Xu:** Supervision, Funding acquisition, Conceptualization.

Declaration of Competing Interest

The authors declare that they have no known competing financial interests or personal relationships that could have appeared to influence the work reported in this paper.

Acknowledgements

References

[1] V. Arutyunov, K. Troshin, A. Nikitin, A. Belyaev, A. Arutyunov, A. Kiryushin, L. Strekova, Selective oxycracking of associated petroleum gas into energy fuel in the light of new data on self-ignition delays of methane-alkane compositions, Chem. Eng. J. 381 (2020) 122706, https://doi.org/10.1016/j.cej.2019.122706.

[2] M. Brennan, CFD simulations of hydrocyclones with an air core: comparison between large eddy simulations and a second moment closure, Chem. Eng. Res. Des. 84 (2006) 495–505, https://doi.org/10.1205/cherd.05111.

[3] B. Cai, J. Wang, L. Sun, N. Zhang, C. Yan, Experimental study and numerical optimization on a vane-type separator for bubble separation in TMSR, Prog. Nucl. Energy 74 (2014) 1–13, https://doi.org/10.1016/j.pnucene.2014.02.007.

[4] X.P. Chen, Investigation on the Flow Characteristics and Rheological Properties of Heavy Crude Oil for Pipeline Transportation, Ph.D. Thesis, University of Chinese Academy, Beijing, 2016.

[5] X. Gao, J. Chen, J. Feng, X.Y. Peng, Numerical and experimental investigations of

[6] F. Gauss, D. Lucas, E. Krepper, Grid studies for the simulation of resolved structures in an Eulerian two-fluid framework, Nucl. Eng. Des. 305 (2016) 371–377, https://doi.org/10.1016/j.nucengdes.2016.06.009.

[7] R. Hreiz, C. Gentric, N. Midoux, R. Lainé, D. Fünfschilling, Hydrodynamics and velocity measurements in gas–liquid swirling flows in cylindrical cyclones, Chem. Eng. Res. Des. 92 (2014) 2231–2246, https://doi.org/10.1016/j.cherd.2014.02.029.

[8] L. Huang, S. Deng, Z. Chen, J.F. Guan, M. Chen, Numerical analysis of a novel gas-liquid pre-separation cyclone, Sep. Purif. Technol. 2018 (2018) 470–479, https://doi.org/10.1016/j.seppur.2017.11.066.

[9] O.S. Ismail, G.E. Umukoro, Modelling combustion reactions for gas flaring and its resulting emissions, J. King Saud. Univ. Eng. Sci. 28 (2) (2016) 130–140, https://doi.org/10.1016/j.jksues.2014.02.003.

[10] J.B.A. Jia, J.B. Babatunde, M. Wang, Void fraction measurement of gas–liquid two-phase flow from differential pressure, Flow Instrum. 41 (2015) 75–80, https://doi.org/10.1016/j.flowmeasinst.2014.10.010.

[11] S. Kanshio, H. Yeung, L. Lao, Study of phase distribution in pipe cyclonic compact separator using wire mesh sensor, Flow Meas, Instrum. 53 (2017) 154–160, https://doi.org/10.1016/j.flowmeasinst.2016.05.003.

[12] A. Korppoo, Russian associated petroleum gas flaring limits: Interplay of formal and informal institutions, Energy policy 116 (2018) 232–241, https://doi.org/10.1016/j.enpol.2018.02.005.

[13] Q. Li, W. Xu, J. Wang, Y.H. Jin, Performance evaluation of a new cyclone separator-Part I experimental results, Sep. Purif. Technol. 141 (2015) 53–58, https://doi.org/10.1016/j.seppur.2014.10.030.

[14] S. Liu, D. Zhang, L.L. Yang, J.Y. Xu, Breakup and coalescence regularity of non-dilute oil drops in a vane-type swirling flow field, Chem. Eng. Res. Des. 129 (2018) 35–54, https://doi.org/10.1016/j.cherd.2017.10.033.

[15] S. Liu, L.L. Yang, Z. Dong, J.Y. Xu, Separation characteristics of the gas and liquid phases in a vane-type swirling flow field, Int. J. Multiphase Flow 107 (2018) 131–145, https://doi.org/10.1016/j.ijmultiphaseflow.2018.05.025.

[16] W. Liu, X.F. Lv, B.F. Bai, Axial development of air–water annular flow with swirl in a vertical pipe, Int. J. Multiphase Flow 124 (2020) 103165, https://doi.org/10.1016/j.ijmultiphaseflow.2019.103165.

[17] Z. Ma, P. Perreault, D.C. Pelegrin, D.C. Boffito, G.S. Patience, Thermodynamically unconstrained forced concentration cycling of methane catalytic partial oxidation over CeO2 FeCralloy catalysts, Chem. Eng. J. 380 (2020) 122470, https://doi.org/10.1016/j.cej.2019.122470.

[18] A. Motin, Theoretical and Numerical Study of Swirling Flow Separation Devices for Oil-Water Mixtures, Michigan State University, Lansing, 2015, p. 2015.

[19] J. Niu, S. Liu, J.Y. Xu, Investigation on separation performance of vane-type gas-liquid tube separator, Chem. Ind. Chem. Eng. Q. (2019) 40, https://doi.org/10.2298/CICEQ190909040N.

[20] R. Sripriya, B.C. Meikap, N. Suresh, S. Chakraborty, D. Bhattacharjee, S. Chandra,

Role of air core in particle separation in cyclones, Miner. Process. Extr. Metall. 122 (1) (2013) 25–35, https://doi.org/10.1179/1743285510Y.0000000004.

[21] L. Sun, L. Zhao, M. Du, J.G. Tang, G. Xie, Performance evaluation of a bubble generator and a bubble separator designed for the gas removal system of a small TMSR, Chin. J. Chem. Eng. (2019), doi:10.1016/j.cjche.2019.01.035 (in press).

[22] M. Wang, R. Mann, F. Dickin, Electrical resistance tomographic sensing systems for industrial applications, Chem. Eng. Commun. 175 (1999) 49–70, https://doi.org/10.1080/00986449908912139.

[23] P. Wei, D. Wang, P. Niu, C.K. Pang, M. Liu, A novel centrifugal gas liquid pipe separator for high velocity wet gas separation, Int. J. Multiphase Flow 124 (2020) 103190, https://doi.org/10.1016/j.ijmultiphaseflow.2019.103190.

[24] J.Y. Xu, M. Wang, Y.X. Wu, H.I. Schlaberg, Z.C. Zheng, R.A. Williams, An experimental study of in-situ phase fraction in jet pump using electrical, resistance

tomography technique, Chin. Phys. Lett. 24 (2007) 512–515 http://cpl.iphy.ac.cn/Y2007/V24/I2/512#1.

[25] X. Xu, Q. Yang, C.Y. Wang, X.L. Ge, H.L. Wang, Dissolved gas separation using the pressure drop and centrifugal characteristics of an inner cone hydrocyclone, Sep. Purif. Technolo. 161 (2016) 121–128, https://doi.org/10.1016/j.seppur.2016.01.006.

[26] J.L. Yin, Y. Qian, Y. Ma, D. Wang, Experimental study on the bubble trajectory in an axial gas-liquid separator applied for tritium removal for molten salt reactors, Nucl. Eng. Des. 320 (2017) 133–140, https://doi.org/10.1016/j.nucengdes.2017.05.015.

[27] T. Yue, J.Y. Chen, J.F. Song, X.H. Chen, Y.A. Wang, Z.H. Jia, R.M. Xu, Experimental and numerical study of upper swirling liquid film (USLF) among gas-liquid cylindrical cyclones (GLCC), Chem. Eng. J. 358 (2019) 806–820, https://doi.org/10.1016/j.cej.2018.10.018.